

CN and CCH derivatives of ethylene and ethane: Confirmation of the detection of CH₃CH₂CCH in TMC-1 [★]

J. Cernicharo¹, B. Tercero^{2,3}, M. Agúndez¹, C. Cabezas¹, R. Fuentetaja¹, N. Marcelino^{2,3}, and P. de Vicente³

¹ Dept. de Astrofísica Molecular, Instituto de Física Fundamental (IFF-CSIC), C/ Serrano 121, 28006 Madrid, Spain.
e-mail: jose.cernicharo@csic.es & marcelino.agundez@csic.es

² Observatorio Astronómico Nacional (OAN, IGN), C/ Alfonso XII, 3, 28014, Madrid, Spain.

³ Centro de Desarrollos Tecnológicos, Observatorio de Yebes (IGN), 19141 Yebes, Guadalajara, Spain.

Received: 07/02/2024; Accepted: 08/03/2024

ABSTRACT

We present a study of CH₃CH₂CCH, CH₃CH₂CN, CH₂CHCCH, and CH₂CHCN in TMC-1 using the QUIJOTE¹ line survey. We confirm the presence of CH₃CH₂CCH in TMC-1, which was previously reported as tentative by our group. From a detailed study of the ethynyl and cyanide derivatives of CH₂CH₂ and CH₃CH₃ in TMC-1, we found that the CH₂CHCCH/CH₂CHCN and CH₃CH₂CCH/CH₃CH₂CN abundance ratios are 1.5±0.1 and 4.8±0.5, respectively. The derived CH₂CHCCH/CH₃CH₂CCH abundance ratio is 15.3±0.8, and that of CH₂CHCN over CH₃CH₂CN is 48±5. All the single substituted isotopologs of vinyl cyanide have been detected, and we found that the first and second carbon substitutions in CH₂CHCN provide a ¹²C/¹³C ratio in line with that found for other three-carbon bearing species such as HCCNC and HNCCC. However, the third ¹³C isotopolog, CH₂CH¹³CN, presents an increase in its abundance similar to that found for HCCCN. Finally, we observed eight *b*-type transitions of CH₂CHCN, and we find that their intensity cannot be fitted adopting the dipole moment μ_b derived previously. These transitions involve the same rotational levels as those of the *a*-type transitions. From their intensity, we obtain $\mu_b=0.80\pm0.03$ D, which is found to be in between earlier values derived in the laboratory using intensity measurements or the Stark effect. Our chemical model indicates that the abundances of CH₃CH₂CCH, CH₃CH₂CN, CH₂CHCCH, and CH₂CHCN observed in TMC-1 can be explained in terms of gas-phase reactions.

Key words. molecular data — line: identification — ISM: molecules — ISM: individual (TMC-1) — astrochemistry

1. Introduction

The ultra-sensitive line survey QUIJOTE¹ performed with the Yebes 40m radio telescope towards the starless cold core TMC-1 (Cernicharo et al. 2021a), together with an ultra-deep line survey of the carbon-rich star IRC+10216 (Pardo et al. 2022), has recently permitted the unambiguous detection of nearly 70 new molecules in space (Cernicharo et al. 2021a; Pardo et al. 2021; Cernicharo et al. 2023a; Cabezas et al. 2023; Cernicharo et al. 2023b, and references therein). Together with the discoveries of the GOTHAM line survey on TMC-1 (McGuire et al. 2018), and the IRAM 30m and Yebes 40m survey of G+0693-0.027 toward the Galactic center (see, e.g., Rivilla et al. 2023), the number of molecules discovered in space has increased from 200 to around 300 species in the past four years, ~70 of which lie in TMC-1. These results place strong constraints on the chemical networks and models of interstellar clouds and on our view on the formation of aromatic rings in these cold objects (McGuire et al. 2018, 2021; Cernicharo et al. 2021b, 2023c; Agúndez et al. 2023a).

TMC-1 is known to harbor abundant cyanopolyynes and the unsaturated carbon-chain radicals C_nH and C_nN. Even vi-

brationally excited C₆H has been found in TMC-1 with the QUIJOTE line survey (Cernicharo et al. 2023d). Nevertheless, the chemistry of this cold core also produces large abundances for more saturated hydrocarbon species such as CH₃CHCH₂ (Marcelino et al. 2007), CH₃CCH (see, e.g., Cabezas et al. 2021; Agúndez et al. 2021, and references therein), CH₂CCH (Agúndez et al. 2021, 2022), vinyl acetylene (Cernicharo et al. 2021b), benzyne (Cernicharo et al. 2021a), cyclopentadiene (Cernicharo et al. 2021c), and indene (Cernicharo et al. 2021c; Burkhardt et al. 2021). In addition, the presence of benzene and naphthalene has been inferred from the detection of their CN and CCH derivatives (McGuire et al. 2018, 2021; Loru et al. 2023). Recently, the CN functionalized forms of indene were also found in the same source by Sita et al. (2022).

In this Letter, we present a systematic study of the ethynyl and cyanide derivatives of ethylene (CH₂CH₂) and ethane (CH₃CH₃) in TMC-1, confirming the previous tentative identification of CH₃CH₂CCH (Cernicharo et al. 2021b). We also report abundances for the singly ¹³C, ¹⁵N, and D substituted isotopologs of CH₂CHCN.

2. Observations

The observational data used in this work are part of QUIJOTE (Cernicharo et al. 2021a), which is a spectral line survey of TMC-1 in the Q band carried out with the Yebes 40m telescope at the position $\alpha_{J2000} = 4^{\text{h}}41^{\text{m}}41.9^{\text{s}}$ and $\delta_{J2000} = +25^{\circ}41'27.0''$, corresponding to the cyanopolyne peak (CP) in TMC-1. The re-

[★] Based on observations with the Yebes 40m radio telescope (projects 19A003, 20A014, 20D023, 21A011, 21D005, 22A007, 22B029, and 23A024) and the IRAM 30m radio telescope. The 40m radio telescope at Yebes Observatory is operated by the Spanish Geographic Institute (IGN, Ministerio de Transportes y Movilidad Sostenible). IRAM is supported by INSU/CNRS (France), MPG (Germany), and IGN (Spain).

¹ Q-band Ultrasensitive Inspection Journey to the Obscure TMC-1 Environment

ceiver was built within the Nanocosmos project² and consists of two cold high-electron mobility transistor amplifiers that cover the 31.0–50.3 GHz band with horizontal and vertical polarizations. The receiver temperatures achieved in the 2019 and 2020 runs vary from 22 K at 32 GHz to 42 K at 50 GHz. Some power adaptation in the down-conversion chains have reduced the receiver temperatures during 2021 to 16 K at 32 GHz and 30 K at 50 GHz. The backends are $2 \times 8 \times 2.5$ GHz fast Fourier transform spectrometers with a spectral resolution of 38 kHz, providing the whole coverage of the Q band in both polarizations. A more detailed description of the system is given by Tercero et al. (2021).

The data of the QUIJOTE line survey presented here were gathered in several observing runs between November 2019 and July 2023. All observations were performed using the frequency-switching observing mode with a frequency throw of 8 and 10 MHz. The total observing time on the source for data taken with frequency throws of 8 MHz and 10 MHz was 737 and 465 hours, respectively. Hence, the total observing time on source was 1202 hours. The measured sensitivity varied between 0.07 mK (70 μ K) at 32 GHz and 0.2 mK at 49.5 GHz. The sensitivity of QUIJOTE is about 50 times better than that of previous line surveys in the Q band of TMC-1 (Kaifu et al. 2004). For each frequency throw, different local oscillator frequencies were used in order to remove possible side-band effects in the down-conversion chain. A detailed description of the QUIJOTE line survey is provided in Cernicharo et al. (2021a). The data analysis procedure has been described by Cernicharo et al. (2022).

The averaged main-beam efficiency measured during our observations varied from 0.66 at 32.4 GHz to 0.50 at 48.4 GHz (Tercero et al. 2021) and can be given across the Q band by $B_{\text{eff}} = 0.797 \exp[-(\nu(\text{GHz})/71.1)^2]$. The averaged forward telescope efficiency is 0.97. The telescope beam size at half-power intensity is 54.4'' at 32.4 GHz and 36.4'' at 48.4 GHz.

We also included in this work data from the 3 mm line survey performed with the IRAM 30m telescope. These data cover the full available band at the telescope, between 71.6 GHz and 117.6 GHz. The EMIR E0 receiver was connected to the Fourier Transform Spectrometers (FTS) in its narrow mode. The FTS provide a spectral resolution of 49 kHz and a total bandwidth of 7.2 GHz per spectral setup. Observations were performed in several runs. Between January and May 2012, we completed the scan 82.5–117.6 GHz (Cernicharo et al. 2012). In August 2018, after the upgrade of the E090 receiver, we extended the survey down to 71.6 GHz. More recent high-sensitivity observations in 2021 were used to improve the signal-to-noise ratio (S/N) in several frequency windows (Agúndez et al. 2022; Cabezas et al. 2022). The final 3mm line survey has a sensitivity of 2–10 mK. However, at some selected frequencies, the sensitivity is as low as 0.6 mK. All the observations were performed using the frequency-switching method with a frequency throw of 7.14 MHz. The IRAM 30m beam varied between 34'' and 21'' at 72 GHz and 117 GHz, respectively, while the beam efficiency took values of 0.83 and 0.78 at the same frequencies, following the relation $B_{\text{eff}} = 0.871 \exp[-(\nu(\text{GHz})/359)^2]$. The forward efficiency at 3 mm is 0.95.

The intensity scale used in this study is the antenna temperature (T_A^*). Calibration was performed using two absorbers at different temperatures and the atmospheric transmission model ATM (Cernicharo 1985; Pardo et al. 2001). The absolute calibration uncertainty was 10%. However, the relative calibration between lines within the QUIJOTE survey is certainly better as

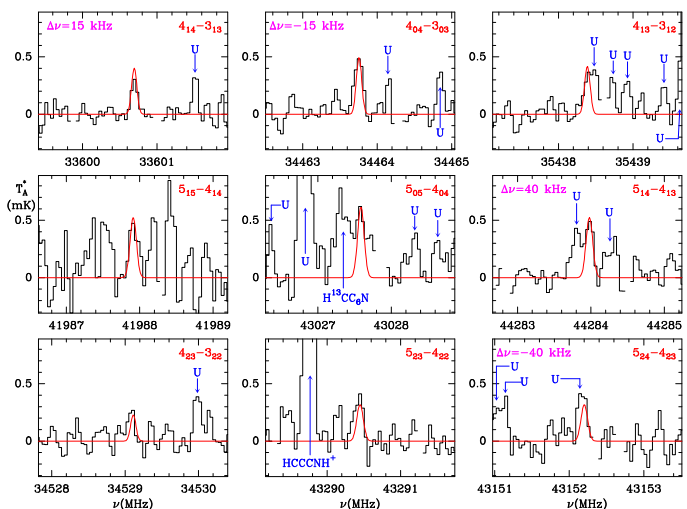


Fig. 1. Observed lines of $\text{CH}_3\text{CH}_2\text{CCH}$ in TMC-1. The line parameters are given in Table A.1. The abscissa corresponds to the rest frequency assuming a velocity for the source of 5.83 km s^{-1} . The ordinate is the antenna temperature corrected for atmospheric and telescope losses in mK. Quantum numbers are indicated in the top right corner of each panel. The red line corresponds to the synthetic spectrum derived from the LTE model described in Sect. 3.1. Blanked channels correspond to negative features produced in the folding of the frequency-switching data. For some lines, we found a frequency shift of up to ± 40 kHz with respect to the predictions (see Sect. 3.1). This is indicated in magenta in the corresponding panels.

all lines were observed simultaneously. The data were analyzed with the GILDAS package³.

3. Results

The line identification was performed using the MADEX code (Cernicharo 2012) and the CDMS and JPL catalogs (Müller et al. 2005; Pickett et al. 1998). The intensity scale used in this study is the antenna temperature (T_A^*). Consequently, the telescope parameters and source properties were used to model the emission of the different species to produce synthetic spectra in this temperature scale. The source was assumed to be circular with a uniform brightness temperature and a radius of 40'' (Fossé et al. 2001). The procedure to derive line parameters is described in Appendix A. To model the observed line intensities, MADEX uses a local thermodynamical equilibrium (LTE) hypothesis supported by rotational diagrams or adopts a large velocity gradient approach (LVG). In the later case, MADEX uses the formalism described by Goldreich & Kwan (1974). Unfortunately, no collisional rates are available for the species studied in this work. The permanent dipolar moments and spectroscopic sources for the molecular species observed in this work are discussed in the next sections.

3.1. $\text{CH}_3\text{CH}_2\text{CCH}$ (ethyl acetylene)

In spite of the large observed abundance of $\text{CH}_3\text{CH}_2\text{CN}$ in hot cores and hot corinos (see Sect. 3.2), the homologous acetylenic form, $\text{CH}_3\text{CH}_2\text{CCH}$, has not been reported in this type of environment so far. The detection is less favorable due to the modest dipole moment ($\mu_a = 0.763 \text{ D}$ and $\mu_b = 0.17 \text{ D}$; Landsberg & Suenram 1983) compared to that of the cyanide form (see Sect. 3.2).

² <https://nanocosmos.iff.csic.es/>

³ <http://www.iram.fr/IRAMFR/GILDAS>

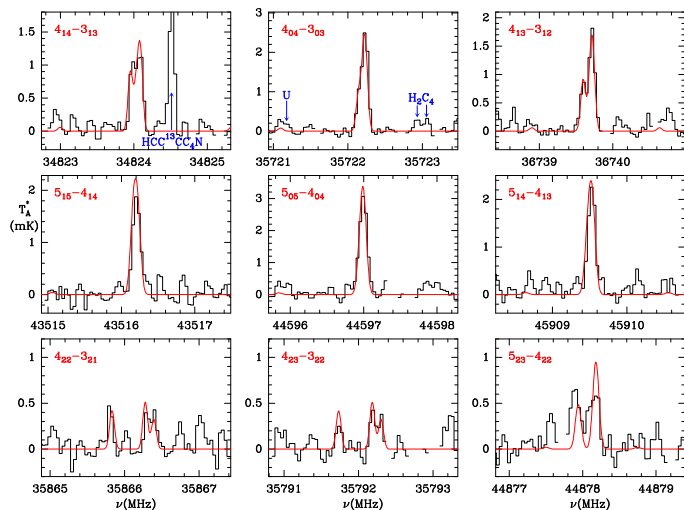


Fig. 2. Observed lines of CH₃CH₂CN in TMC-1. The line parameters are given in Table A.1. The abscissa corresponds to the rest frequency assuming a velocity for the source of 5.83 km s⁻¹. The ordinate is the antenna temperature corrected for atmospheric and telescope losses in mK. Quantum numbers are indicated in the top left corner of each panel. The red line corresponds to the synthetic spectrum derived from the model described in Sect. 3.2. Blanked channels correspond to negative features produced in the folding of the frequency-switching data.

We recently reported a tentative detection of this species toward the cold starless core TMC-1. The claim was based on the observation of a few lines and a spectral stacking of all the transitions in the QUIJOTE line survey (Cernicharo et al. 2021b). Here, we present the detection of nine lines of the molecule, including some $K_a=2$ transitions. The data are shown in Fig. 1, and their line parameters are given in Table A.1. The laboratory data for the rotational spectroscopy of this species were summarized by Steber et al. (2012). We note, however, that in the microwave domain, Bestmann & Dreizler (1985) reported a small internal rotation splitting of about 100 kHz, but the uncertainty of their measurements was on the same order. Although the laboratory data cover high quantum numbers (up to $J=46$ and $K=28$) and the frequency predictions should be accurate enough in the QUIJOTE band, our observations show frequency shifts with respect to the predictions of up to 40 kHz (our channel width) for four transitions (indicated in magenta in Fig. 1 in the top left corner of the panels). This difference is compatible with the uncertainties of the laboratory measurements in the Q band and with the possible splitting between the A and E symmetry species at these frequencies. To derive the column density of this molecule, we assumed a rotational temperature of 9 K. This assumption was based on the low dipole moment of the molecule and on the results we obtained for CH₂CHCCH (see Sect. 3.3 and Cernicharo et al. 2021b). The derived value is $N = (6.2 \pm 0.2) \times 10^{11}$ cm⁻² (see Table 1). Using the column density derived in Sect. 3.3 for vinyl acetylene, we obtain a CH₂CHCCH/CH₃CH₂CCH abundance ratio of 15.3 ± 0.8 .

3.2. CH₃CH₂CN (ethyl cyanide)

CH₃CH₂CN and several of its vibrationally excited states exhibit a dense spectrum in warm molecular clouds such as Orion-KL and SgrB2 (Johnson et al. 1977; Gib et al. 2000; Daly et al. 2013; Margulès et al. 2018). However, the molecule was not detected in cold dark clouds until recently, when we reported several of its rotational lines toward TMC-1 (Cernicharo et al.

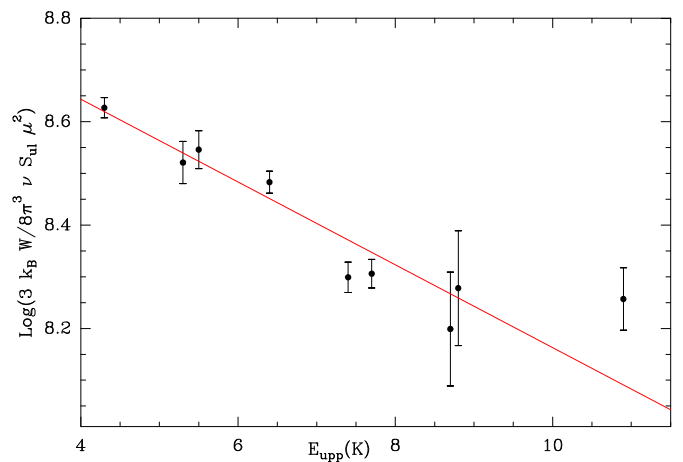


Fig. 3. Rotational diagram of the observed lines of CH₃CH₂CN from the data of Table A.1. A rotational temperature of 5.5 ± 0.5 K is derived.

Table 1. Derived column densities and abundances

Species	T_{rot} (K)	N (cm ⁻²)	X^a	
CH ₃ CH ₂ CCH	9.0	$(6.2 \pm 0.2) \times 10^{11}$	6.2×10^{-11}	A
CH ₃ CH ₂ CN	5.5 ± 0.5	$(1.3 \pm 0.1) \times 10^{11}$	1.3×10^{-11}	
CH ₂ CHCCH	10.4 ± 0.9	$(9.5 \pm 0.2) \times 10^{12}$	9.5×10^{-09}	B
CH ₂ CHCN	4.3 ± 0.2	$(6.2 \pm 0.2) \times 10^{12}$	6.2×10^{-09}	
¹³ CH ₂ CHCN	4.3	$(6.2 \pm 0.2) \times 10^{10}$	6.2×10^{-12}	C
CH ₂ ¹³ CHCN	4.3	$(5.9 \pm 0.2) \times 10^{10}$	5.9×10^{-12}	C
CH ₂ CH ¹³ CN	4.3	$(8.1 \pm 0.3) \times 10^{10}$	8.1×10^{-12}	C
CH ₂ CDCN	4.3	$(4.7 \pm 0.3) \times 10^{10}$	4.7×10^{-12}	C
<i>trans</i> -CHDCHCN	4.3	$(4.5 \pm 0.3) \times 10^{10}$	4.5×10^{-12}	C
<i>cis</i> -CHDCHCN	4.3	$(4.9 \pm 0.3) \times 10^{10}$	4.9×10^{-12}	C
CH ₂ CHC ¹⁵ N	4.3	$(2.2 \pm 0.2) \times 10^{10}$	2.2×10^{-12}	C

Notes. ^(a) We assumed $N(\text{H}_2) = 10^{22}$ cm⁻² to derive the molecular abundances (Cernicharo & Guélin 1987). ^(A) We assumed that the molecule is thermalized at the kinetic temperature of the cloud (9 K; see text). ^(B) A rotational diagram provides $T_{rot} = 10.5 \pm 1.5$. We assumed that the molecule is thermalized at the kinetic temperature of the cloud (9 K; see text). ^(C) Rotational temperature assumed to be identical to that of the main isotopolog.

2021b). In this work, we present the spectra for this species using the latest QUIJOTE data. The spectroscopic laboratory frequency measurements are from Fukuyama et al. (1996) and Brauer et al. (2009), from which we derived the rotational and distortion constants and implemented them in MADEX. Nine a -type lines were detected, and they are shown in Fig. 2, while their line parameters are given in Table A.1. Some of the $K_a=1$ and all $K_a=2$ lines show hyperfine structure. The frequencies including hyperfine structure were adopted from the CDMS catalog (Müller et al. 2005). A rotational diagram analysis of the data provided a rotational temperature of 5.5 ± 0.5 K (see Fig. 3) and a column density of $(1.3 \pm 0.1) \times 10^{11}$ cm⁻². The abundance ratio of CH₃CH₂CCH and ethyl cyanide in TMC-1 is 4.8 ± 0.5 . Although the frequencies of the ¹³C, ¹⁵N, and D isotopologs of ethyl cyanide are well known (Demyk et al. 2007; Richard et al. 2012; Margulès et al. 2009), the intensity of the lines of the main isotopolog indicates that the lines from these isotopologs will be well below the current sensitivity limit of the QUIJOTE line survey.

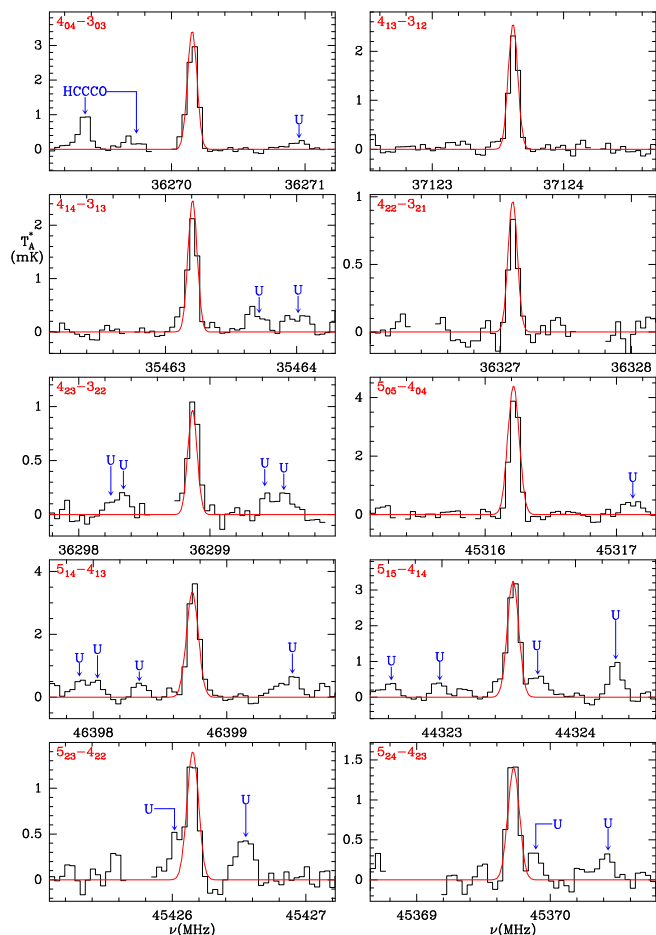


Fig. 4. Observed lines of CH_2CHCCH in TMC-1. The line parameters are given in Table A.1. The abscissa corresponds to the rest frequency assuming a velocity for the source of 5.83 km s^{-1} . The ordinate is the antenna temperature corrected for atmospheric and telescope losses in mK. Quantum numbers are indicated in the top left corner of each panel. The red line corresponds to the synthetic spectrum derived from the model described in Sect. 3.3. Blanked channels correspond to negative features produced in the folding of the frequency-switching data.

3.3. CH_2CHCCH (vinyl acetylene)

In spite of the similarity in structure with CH_2CHCN , which has been detected toward different astrophysical environments (see Sect. 3.4), vinyl acetylene was only recently detected through the sensitivity of the QUIJOTE line survey (Cernicharo et al. 2021b). Due to the small dipole moment of the molecule ($\mu_a=0.43 \text{ D}$, $\mu_b \sim 0$, Sobolev et al. 1962; Thorwirth & Lichau 2003), the derived abundance was rather large ($\sim 10^{13} \text{ cm}^{-2}$). The rotational spectroscopy in the laboratory for this species was summarized by Thorwirth & Lichau (2003) and Thorwirth et al. (2004). The observed lines in our study are shown in Fig. 4, and their parameters are given in Table A.1. A rotational diagram analysis of the data provides $T_{\text{rot}}=10.4 \pm 0.9 \text{ K}$ (see Fig. 5), which is compatible with a thermalized molecule at the kinetic temperature of the cloud, as expected for a species with a low dipole moment ($T_K=9 \text{ K}$; Agúndez et al. 2023b). The derived column density is $(9.5 \pm 0.2) \times 10^{12} \text{ cm}^{-2}$, which agrees well with the value we reported previously. The derived $\text{CH}_2\text{CHCCH}/\text{CH}_2\text{CHCN}$ abundance ratio is 1.5 ± 0.1 .

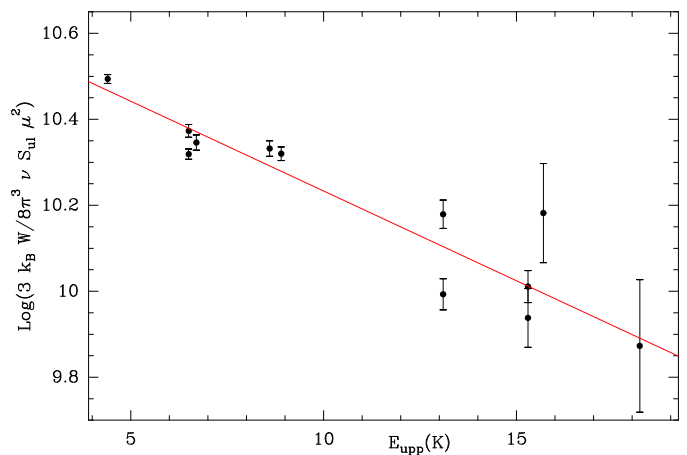


Fig. 5. Rotational diagram of the observed lines of CH_2CHCCH from the data of Table A.1, including the lines observed at 3mm. A rotational temperature of $10.4 \pm 0.9 \text{ K}$ is derived.

3.4. CH_2CHCN (vinyl cyanide; acrylonitrile)

CH_2CHCN was detected in the early years of astrochemistry toward SgrB2 (Gardner & Winnewisser 1975). The molecule was detected toward TMC-1 by Matthews & Seers (1981) and more recently by Cernicharo et al. (2021b). Vinyl cyanide was also detected toward the carbon-rich star IRC+10216 (Agúndez et al. 2008) and in high-mass star-forming regions (Belloche et al. 2013; López et al. 2014). There is a large set of laboratory data on the rotational spectroscopy of this species that covers frequencies up to 1.67 THz, $J=129$, and $K_a=28$ (Müller et al. 2008; Kisiel et al. 2009, and references therein). The frequency predictions have uncertainties lower than 1 kHz in the frequency domains covered in this study.

We have observed 23 a -type and 8 b -type transitions of CH_2CHCN in the 7 mm and the 3 mm domains. Several of these lines exhibit well-resolved hyperfine components. The lines observed in the Q band are shown in Fig. 6. The line parameters for all observed lines are given in Table A.1. A rotational diagram is shown in Fig. 7. The initial dipole moments used in the analysis of the data were those measured by Stolze & Sutter (1985) ($\mu_a = 3.815 \text{ D}$ and $\mu_b = 0.894 \text{ D}$). The a - and b -type transitions are well fit with a common rotational temperature of $4.3 \pm 0.2 \text{ K}$. However, the column density derived from the b -type transitions is a factor 1.3 times lower than the corresponding density from the a -type transitions. The effect is systematic as all b -type transitions are well reproduced with a common column density. This discrepancy cannot be attributed to a calibration problem of the data. All a - and b -type lines were observed with the same set of observational data, gathered at the same time, and with the same systematics. Moreover, the same upper levels are involved in both transition types. It cannot be due to an opacity problem because for the strongest a -type transitions, we estimate opacities ~ 0.15 . Hence, it seems that the relative value of the dipole moments is not well determined.

The dipole moment of acrylonitrile has been the subject of several laboratory studies. The first determination was made by Wilcox & Goldstein (1954), who derived $\mu_a = 3.68 \text{ D}$ and $\mu_b = 1.25 \text{ D}$. Subsequent measurements by Stolze & Sutter (1985) provided different values, $\mu_a = 3.815 \pm 0.012 \text{ D}$ and $\mu_b = 0.894 \pm 0.068 \text{ D}$. The more recent determination of $\mu_b = 0.687 \pm 0.008 \text{ D}$ (Krańnicki & Kisiel 2011) produced the reverse, that is, the column density from b -type transitions is 1.3 times higher than the value derived from the a -type tran-

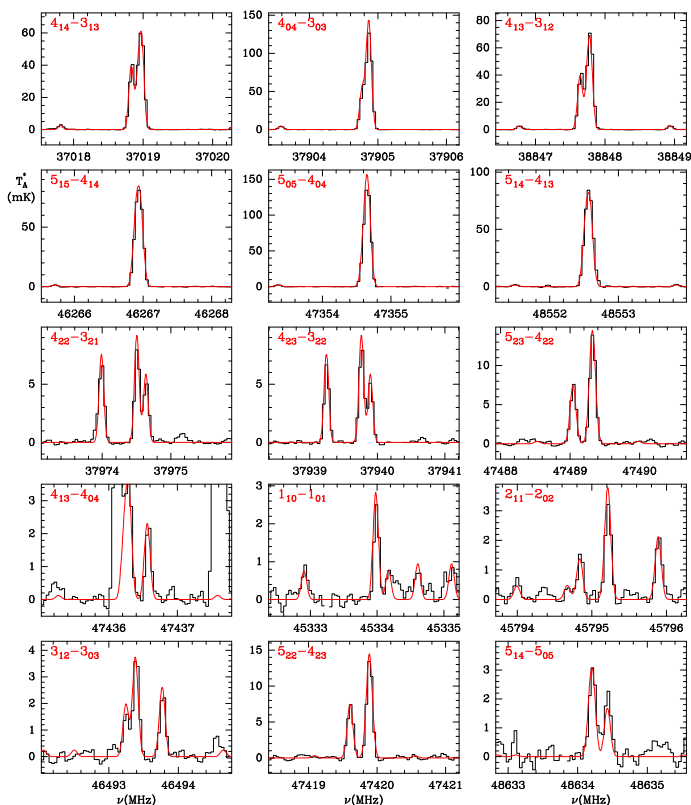


Fig. 6. Observed lines of CH₂CHCN in TMC-1. The line parameters are given in Table A.1. The abscissa corresponds to the rest frequency assuming a velocity for the source of 5.83 km s⁻¹. The ordinate is the antenna temperature corrected for atmospheric and telescope losses in mK. Quantum numbers are indicated in the top left corner of each panel. The red line corresponds to the synthetic spectrum derived from the model described in Sect. 3.4. Blanked channels correspond to negative features produced in the folding of the frequency switching data. The $J_u=4,5$ ($K_a=0,1$) transitions of the isotopologs of CH₂CHCN are detected and are shown in Fig. 8.

sitions. To coherently interpret our data, we fit the value of μ_b necessary to produce similar column densities for both types of transitions keeping μ_a to the value derived by Stolze & Sutter (1985). We obtain a value of 0.80 ± 0.03 D, which is between the two experimental determinations. The rotational diagram shown in Fig. 7 permits us to simultaneously fit all transitions with $T_{rot} = 4.3 \pm 0.2$ K and a column density for acrylonitrile of $(6.2 \pm 0.2) \times 10^{12}$ cm⁻² (see also Cernicharo et al. 2021b). The computed synthetic spectra are presented in Fig. 6 and agree excellently with all the observed transitions, *b* and *a* type.

Rotational spectroscopy for the ¹³C, ¹⁵N, and deuterated isotopologs of acrylonitrile was performed by Colmont et al. (1997); Müller et al. (2008); Kisiel et al. (2009), and Krašnicki et al. (2011). The ¹³C isotopologs were detected toward Sgr B2 (Müller et al. 2008) and Orion-KL (López et al. 2014). In our study of TMC-1, we detected six *a*-type transitions for the three ¹³C substituted isotopologs, some of which exhibit the corresponding hyperfine splitting. We also solidly detected the isotopologs CH₂CHC¹⁵N, CH₂CDCN, *trans*-CHDCHCN, and *cis*-CHDCHCN (all these lines are *a* type) for the first time in the ISM. A tentative detection in Orion-KL of the deuterated species was previously reported (López et al. 2014), but the detection was based on a small number of weak lines with severe overlap with lines from other molecular species. The lines observed toward TMC-1 are shown in Fig. 8. In their analysis, we

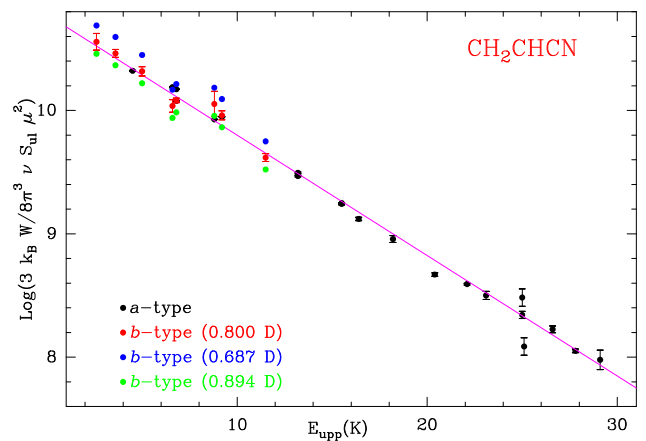


Fig. 7. Rotational diagram of the observed lines of CH₂CHCN. The black and red points correspond to *a*-type and *b*-type transitions, respectively. A rotational temperature of 4.3 ± 0.2 K is derived. The estimated *b*-component of the dipolar moment is 0.80 ± 0.03 D. The blue and green points correspond to the *b*-type transitions when using $\mu_b = 0.687$ D (Krašnicki & Kisiel 2011) and 0.894 D (Stolze & Sutter 1985), respectively. Their error bars are identical to those of the red points.

adopted the same rotational temperature and dipole moments as for the main isotopolog. The derived column densities for all the isotopologs are given in Table 1. The three singly deuterated species show similar column densities and a deuterium enhancement ~ 130 , which is significantly lower than was found in other species (Cernicharo et al. 2024; Tercero et al. 2024). The first and second ¹³C isotopologs show a ¹²C/¹³C abundance ratio of 100 ± 7 , while for the substitution in the third position, the ratio is 76 ± 5 . The CH₂CHCN/CH₂CHC¹⁵N abundance ratio is 282 ± 35 . These values are in line with those derived for HCCCN by Tercero et al. (2024) and HNCCC and HCCNC by Cernicharo et al. (2024). These two papers provide a detailed discussion of the ¹³C enhancement in these species.

4. Discussion

The observational data presented here make it worthwhile to revisit the chemistry of the CCH and CN derivatives of CH₂CH₂ and CH₃CH₃. We carried out chemical modeling calculations using a gas-phase chemical model. The model was essentially the same as presented previously in Cernicharo et al. (2021b). Briefly, we adopted typical parameters of cold dark clouds, that is, a gas kinetic temperature of 10 K, a volume density of H₂ of 2×10^4 cm⁻³, a cosmic-ray ionization rate of H₂ of 1.3×10^{-17} s⁻¹, a visual extinction of 30 mag, and the so-called low metal elemental abundances (Agúndez & Wakelam 2013). The core of the chemical network is based on the RATE12 network from the UMIST database (McElroy et al. 2013), with some updates from the more recent literature (e.g., Loison et al. 2015). The relevant reactions that describe the formation of the CCH and CN derivatives of CH₂CH₂ and CH₃CH₃ are discussed below. The calculated fractional abundances of CH₂CHCCH, CH₂CHCN, CH₃CH₂CCH, and CH₃CH₂CN are shown as a function of time in Fig. 9. The chemical model produces abundances at times of a few 10⁵ yr that are in reasonable good agreement with the observed values, with discrepancies one order of magnitude or smaller. Taking into account that the chemistry of these four molecules is not particularly well known, we can consider that the agreement between observations and model is satisfactory,

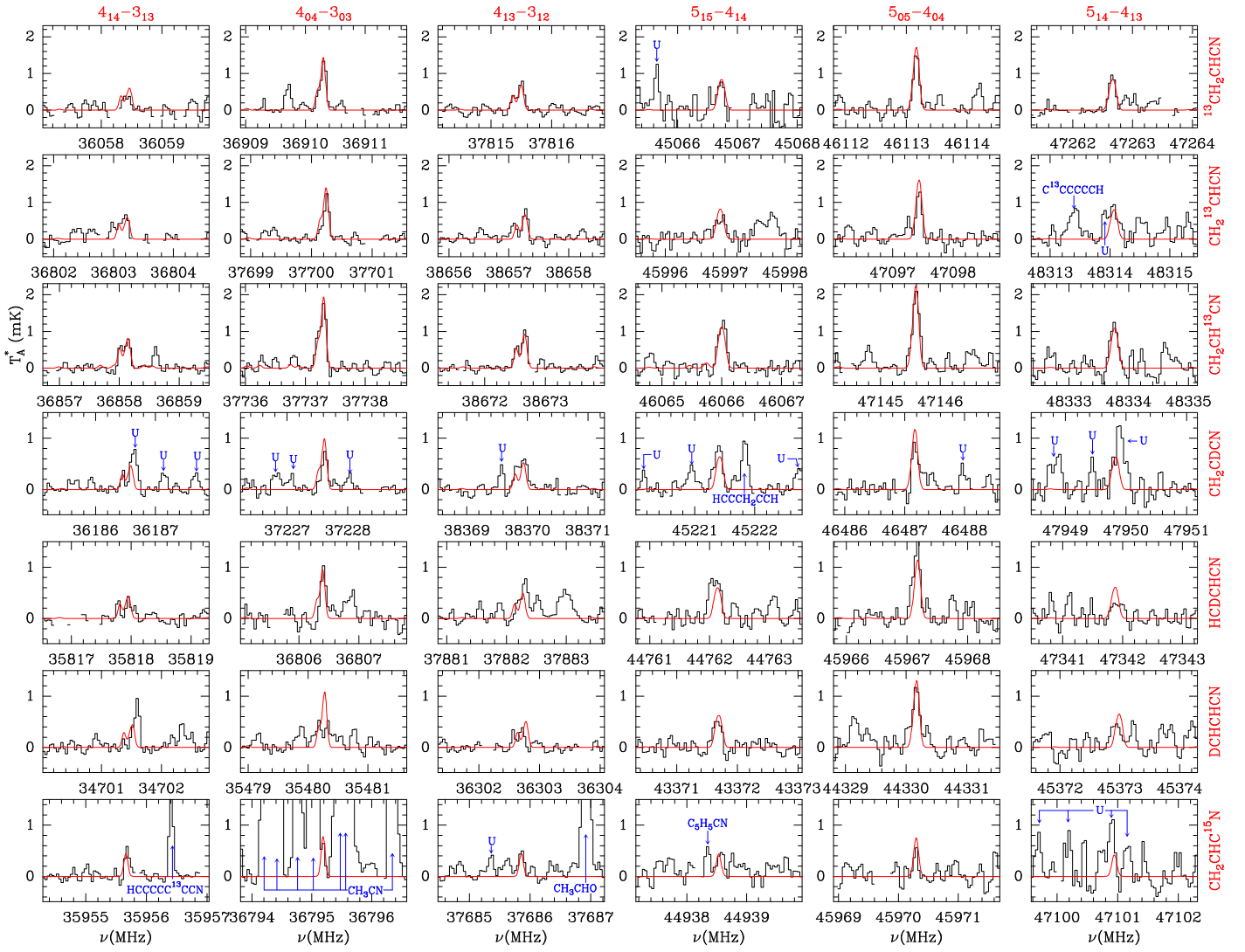


Fig. 8. Observed lines of the isotopologs of CH_2CHCN . The line parameters are given in Table A.1. The abscissa corresponds to the rest frequency assuming a velocity for the source of 5.83 km s^{-1} . The ordinate is the antenna temperature corrected for atmospheric and telescope losses in mK. The species are indicated at the end of each row, and the quantum numbers are indicated at the top of each column. The red line corresponds to the synthetic spectrum derived from the model described in Sect. 3.4. Blanked channels correspond to negative features produced in the folding of the frequency-switching data.

although a better knowledge of the reactions of formation and destruction of these molecules is highly desirable.

The CCH and CN derivatives of C_2H_4 are formed in the chemical model through the reactions of C_2H and CN with C_2H_4 , which are rapid and proceed through H atom elimination, according to an extensive number of studies (Opansky & Leone 1996; Vakhtin et al. 2001; Bouwman et al. 2012; Krishtal et al. 2009; Dash & Rajakumar 2015; Sims et al. 1993; Choi et al. 2004; Gannon et al. 2007; Balucani et al. 2015). In addition, CH_2CHCCH is also formed by the reaction of CH with CH_3CCH and CH_2CCH_2 (Daugey et al. 2005; Goulay et al. 2009; Ribeiro & Mebel 2017) and by the reaction $\text{C}_2 + \text{C}_2\text{H}_6$ (Páramo et al. 2008), although this latter reaction probably occurs through H abstraction, in which case, it would not produce CH_2CHCCH . On the other hand, CH_2CHCN is also produced in the reaction $\text{CN} + \text{CH}_2\text{CHCH}_3$ (Sims et al. 1993; Morales et al. 2010; Gannon et al. 2007; Huang et al. 2009) and in the dissociative recombination of the cation $\text{C}_3\text{H}_4\text{N}^+$, although for this latter process, the branching ratios for the different fragmentation products are unknown.

In the case of the CCH and CN derivatives of C_2H_6 , the formation pathways are more uncertain. The most obvious chemical route would be $\text{CCH} + \text{C}_2\text{H}_6$ and $\text{CN} + \text{C}_2\text{H}_6$. These reactions are fast (Opansky & Leone 1996; Sims et al. 1993), but occur through H abstraction rather than H elimination (Dash & Rajakumar 2015; Georgievskii & Klippenstein 2007; Espinosa-García & Rangel 2023). The main routes to $\text{CH}_3\text{CH}_2\text{CCH}$ in the model are the dissociative recombination of C_4H_7^+ and $\text{CH} + \text{CH}_2\text{CHCH}_3$. This latter reaction was measured to be rapid at low temperatures (Daugey et al. 2005), and the reaction was found to occur mostly through H elimination (Loison & Bergeat 2009). Trevitt et al. (2013) reported that $\text{CH}_3\text{CH}_2\text{CCH}$ is produced with a branching ratio of 0.12, although theoretical calculations (Ribeiro & Mebel 2016; He et al. 2019) pointed to 1,2-butadiene as the only C_4H_6 isomer formed. For $\text{CH}_3\text{CH}_2\text{CN}$, the only formation channel in the model is the dissociative recombination of $\text{C}_3\text{H}_6\text{N}^+$, although it is unknown how large cations, such as C_4H_7^+ and $\text{C}_3\text{H}_6\text{N}^+$, fragment upon reaction with electrons.

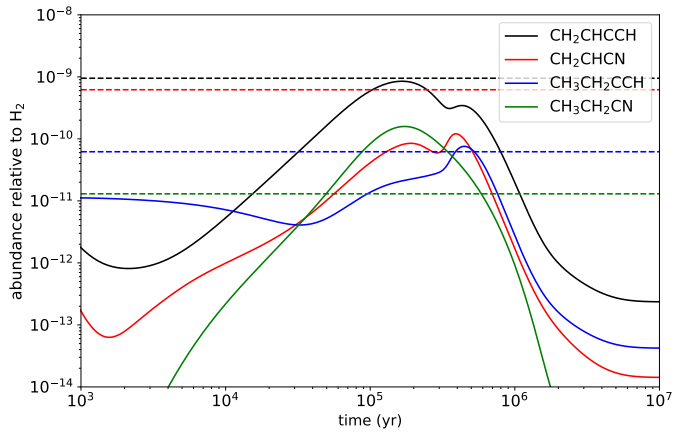


Fig. 9. Calculated fractional abundances of the CCH and CN derivatives of C₂H₄ and C₂H₆ as a function of time. The horizontal dashed lines correspond to the abundances observed in TMC-1.

In summary, the formation of CH₂CHCCH, CH₂CHCN, CH₃CH₂CCH, and CH₃CH₂CN in TMC-1 can be explained in terms of standard gas-phase routes involving neutral-neutral and ion-neutral reactions. However, there are still important uncertainties regarding the different products resulting from the various possible reactions of formation of these molecules.

Acknowledgements. We thank Ministerio de Ciencia e Innovación of Spain (MICIU) for funding support through projects PID2019-106110GB-I00, and PID2019-106235GB-I00, PID2022-137980NB-I00, MCIN/AEI/10.13039/501100011033. We thank the Consejo Superior de Investigaciones Científicas (CSIC) for funding through project PIE 202250I097. We also thank ERC for funding through grant ERC-2013-Syg-610256-NANOCOSMOS.

References

Agúndez, M., Fonfría, J.P., Cernicharo, J. et al. 2008, *A&A*, 479, 493
 Agúndez, M. & Wakelam, V. 2013, *Chem. Rev.*, 113, 8710
 Agúndez, M., Cabezas, C., Tercero, B. et al. 2021, *A&A*, 647, L10
 Agúndez, M., Marcelino, N., Cabezas, C. et al. 2022, *A&A*, 657, A96
 Agúndez, M., Marcelino, N., Tercero, B. et al. 2023a, *A&A*, 677, L13
 Agúndez, M., Marcelino, N., Tercero, B. et al. 2023b, *A&A*, 677, A106
 Balucani, N., Leonori, F., Petrucci, R., et al. 2015, *Chem. Phys.*, 449, 34
 Belloche, A., Müller, H.S.P., Menten, K.M. et al. 2013, *A&A*, 559, A47
 Bestmann, G. & Dreizler, H. 1985, *Z. Naturforsch.*, 40a, 263
 Bouwman, J., Goulay, F., Leone, S. R., & Wilson, K. R. 2012, *J. Phys. Chem. A*, 116, 3907
 Brauer, C.S., Pearson, J.C., Drouin, B.J. & Yu, S. 2009, *ApJS*, 184, 133
 Burkhardt, A.M., Long Kelvin Lee, K., Changala, P.B. et al. 2021, *ApJ*, 913, L18
 Cabezas, C., Endo, Y., Roueff, E., et al. 2021, *A&A*, 646, L1
 Cabezas, C., Agúndez, M., Marcelino, N., et al. 2022, *A&A*, 657, L4
 Cabezas, C., Agúndez, M., Marcelino, N., et al. 2023, *A&A*, 676, L5
 Cernicharo, J. 1985, Internal IRAM report (Granada: IRAM)
 Cernicharo, J. & Guélin, M. 1987, *A&A*, 176, 299
 Cernicharo, J., 2012, in *ECLA 2011: Proc. of the European Conference on Laboratory Astrophysics*, EAS Publications Series, 2012, Ed.: C. Stehl, C. Joblin, & L. d'Hendecourt (Cambridge: Cambridge Univ. Press), 251; https://nanocosmos.iff.csic.es/?page_id=1619
 Cernicharo, J., Marcelino, N., Roueff, E., et al. 2012, *ApJ*, 759, L43
 Cernicharo, J., Marcelino, N., Agúndez, M. et al. 2020, *A&A*, 642, L8
 Cernicharo, J., Agúndez, M., Kaiser, R., et al. 2021a, *A&A*, 652, L9
 Cernicharo, J., Agúndez, M., Cabezas, C. et al. 2021b, *A&A*, 647, L2
 Cernicharo, J., Agúndez, M., Cabezas, C. et al. 2021c, *A&A*, 649, L15
 Cernicharo, J., Fuentetaja, R., Agúndez, M. et al. 2022, *A&A*, 663, L9
 Cernicharo, J., Pardo, J. R., Cabezas, C. et al. 2023a, *A&A*, 670, L19
 Cernicharo, J., Cabezas, C., Pardo, J.R. et al. 2023b, *A&A*, 672, L13
 Cernicharo, Tercero, B., Marcelino, N. et al. 2023c, *A&A*, 674, L4
 Cernicharo, J., Fuentetaja, R., Agúndez, M. et al. 2023d, *A&A*, 680, L4
 Cernicharo, J., et al. 2024, *A&A*, in press, 10.48550/arXiv.2401.15997
 Choi, N., Blitz, M. A., McKee, K., et al. 2004, *Chem. Phys. Lett.*, 384, 68

Colmont, J.M., Wlodarczak, G., Priem, D. et al. 1997, *J. Mol. Spectrosc.*, 181, 330
 Daly, A.M., Bermúdez, C., López, A. et al. 2013, *A&A*, 568, A81
 Dash, M. R. & Rajakumar, B. 2015, *PCCP*, 17, 3142
 Daugey, N., Caubet, P., Retail, B., et al. 2005, *PCCP*, 7, 2921
 Demyk, K., Mäder, H., Tercero, B. et al. 2007, *A&A*, 466, 255
 Espinosa-García, J. & Rangel, C. 2023, *J. Chem. Phys.*, 159, 124307
 Fossé, D., Cernicharo, J., Gerin, M., Cox, P. 2001, *ApJ*, 552, 168
 Fukuyama, Y., Odashima, H., Takagi, K. & Tsunekawa, S. 1996, *ApJS*, 104, 329
 Gannon, K. L., Glowacki, D. R., Blitz, M. A., et al. 2007, *J. Phys. Chem. A*, 111, 6679
 Gardner, F.F. & Winnewisser, G. 1975, *ApJ*, 195, L127
 Georgievskii, Y. & Klippenstein, S. J. 2007, *J. Phys. Chem.*, 111, 3802
 Goulay, F., Trevitt, A. J., Meloni, G., et al. 2009, *J. Am. Chem. Soc.*, 131, 993
 Gib, E., Nummelin, A., Irvine, W.M. et al. 2000, *ApJ*, 545, 309
 Goldreich, P. & Kwan, J. 1974, *ApJ*, 189, 441
 He, C., Thomas, A. M., Galimova, G. R., et al. 2019, *J. Phys. Chem. A*, 123, 10543
 Huang, C. H., Kaiser, R. I., & Chang, A. H. H. 2009, *J. Phys. Chem. A*, 113, 12675
 Johnson, D. R., Lovas, F. J., Gottlieb, C. A. et al. 1977, *ApJ*, 218, L370
 Kaifu, N., Ohishi, M., Kawaguchi, K., et al. 2004, *PASJ*, 56, 69
 Kisiel, Z., Pszczółkowski, L.-Drouin, B.J. et al. 2009, *J. Mol. Spectrosc.*, 258, 26
 Kraśnicki, A. & Kisiel, Z. 2011, *J. Mol. Spectrosc.*, 270, 83
 Kraśnicki, A., Kisiel, Z., Drouin, B.J. et al., 2011, *J. Mol. Struct.*, 1006, 20
 Krishal, S. P., Mebel, A. M., & Kaiser, R. I. 2009, *J. Phys. Chem. A*, 113, 11112
 Landsberg, B.M. & Suenram, R.D. 1983, *J. Mol. Spectrosc.*, 98, 210
 Loison, J.-C. & Bergeat, A. 2009, *PCCP*, 11, 655
 Loison, J.-C., Hébrard, E., Dobrijevic, M., et al. 2015, *Icarus*, 247, 218
 López, A., Tercero, B., Kisiel, Z. et al. 2014, *A&A*, 572, A44
 Loru, D., Cabezas, C., Cernicharo, J. et al., 2023, *A&A*, 677, A166
 Marcelino, N., Cernicharo, J., Agúndez, M. et al. 2007, *ApJ*, 665, L127
 Margulès, L., Motiyenko, R., Demyk, K. et al. 2009, *A&A*, 493, 565
 Margulès, L., Tercero, B., Guillemin, J.C. et al. 2018, *A&A*, 610, A44
 Matthews, H.E & Sears, T.J. 1981, *ApJ*, 272, 149
 McElroy, D., Walsh, C., Markwick, A. J., et al. 2013, *A&A*, 550, A36
 McGuire, B.A., Burkhardt, A.M., Kalenskii, S., et al. 2018, *Science*, 359, 202
 McGuire, B.A., Loomis, R.A., Burkhardt, A.M., et al. 2021, *Science*, 371, 1265
 Morales, S. B., Le Picard, S. D., Canosa, A., & Sims, I. R. 2010, *Faraday Discuss.*, 147, 155
 Müller, H. S. P., Schlöder, F., Stutzki, J., Winnewisser, G. 2005, *J. Mol. Struct.*, 742, 215
 Müller, H. S. P., Belloche, A., Menten, K. et al. 2008, *J. Mol. Spectrosc.*, 251, 319
 Opansky, B. J. & Leone, S. R. 1996, *J. Phys. Chem.*, 100, 19904
 Páramo, A., Canosa, A., Le Picard, S. D., & Sims, I. R. 2008, *J. Phys. Chem. A*, 112, 9591
 Pardo, J. R., Cernicharo, J., Serabyn, E. 2001, *IEEE Trans. Antennas and Propagation*, 49, 12
 Pardo, J. R., Cabezas, C., Fonfría, J.P. et al. 2021, *A&A*, 652, L13
 Pardo, J. R., Cernicharo, J., Tercero, B. et al. 2022, *A&A*, 658, A39
 Pickett, H. M., Poynter, R. L., Cohen, E. A., et al. 1998, *J. Quant. Spectrosc. Radiat. Transfer*, 60, 883
 Ribeiro, J. M. & Mebel, A. M. 2016, *J. Phys. Chem. A*, 120, 1800
 Ribeiro, J. M. & Mebel, A. M. 2017, *PCCP*, 19, 14543
 Richard, C., Margulès, L., Motiyenko, R. & Guillemin, J.-C. 2012, *A&A*, 543, A135
 Rivilla, V.M., Sanz-Novo, M., Jiménez-Serra, I. et al. 2023, *ApJ*, 953, L20
 Sims, I. R., Queffelec, J.-L., Travers, D., et al. 1993, *Chem. Phys. Lett.*, 211, 461
 Sita, M.L., Changala, P.B., Xue, C. et al. 2022, *ApJ*, 938, L12
 Sobolev, G. A., Shcherbakov, A. M., & Akishin, P. A. 1962, *Opt. Spectrosc.*, 12, 78
 Steber, A. L., Harris, B. J., Neill, J. L. et al. 2012, *J. Mol. Spectrosc.*, 280, 3
 Stolze, M. & Sutter, D.H. 1985, *Z. Naturforsch.*, 40a, 998
 Tercero, F., López-Pérez, J. A., Gallego, et al. 2021, *A&A*, 645, A37
 Tercero, B. et al. 2024, *A&A*, in press, 10.48550/arXiv.2402.01318
 Thorwirth, S., & Lichau, H. et al. 2003, *A&A*, 398, L11
 Thorwirth, S., Müller, H. S. P., Lichau, H. et al. 2004, *J. Mol. Struct.*, 695, 263
 Trevitt, A. J., Prendergast, M. B., Goulay, F., et al. 2013, *J. Phys. Chem. A*, 117, 6450
 Vakhtin, A. B., Heard, D. E., Smith, I. W. M., & Leone, S. R. 2001, *Chem. Phys. Lett.*, 348, 21
 Wilcox, W. S. & Goldstein, J. H. 1954, *J. Chem. Phys.*, 22, 516

Appendix A: Line parameters

The line parameters for all observed transitions with the Yebes 40m and IRAM 30m radio telescopes were derived by fitting a Gaussian line profile to them using the GILDAS package. A velocity range of $\pm 20 \text{ km s}^{-1}$ around each feature was considered for the fit after a polynomial baseline was removed. Negative features produced in the folding of the frequency switching data were blanked before baseline removal.

Table A.1. Observed line parameters for the species.

Molecule	J^a	F^b	ν_{rest}^c (MHz)	$\int T_A^* dv^d$ (mK km s $^{-1}$)	v_{LSR}^e (km s $^{-1}$)	Δv^f (km s $^{-1}$)	$T_A^* g$ (mK)	Notes
CH ₃ CH ₂ CCH	4 _{1,4} – 3 _{1,3}		33600.696±0.020	0.27±0.05	5.83±0.00	0.83±0.18	0.31±0.06	
	4 _{0,4} – 3 _{0,3}		34463.749±0.020	0.61±0.07	5.83±0.00	1.15±0.15	0.50±0.06	
	4 _{2,3} – 3 _{2,2}		34529.087±0.030	0.27±0.09	5.83±0.00	0.92±0.25	0.28±0.09	
	4 _{1,3} – 3 _{1,2}		35438.395±0.020	0.31±0.07	5.83±0.00	0.80±0.00	0.36±0.08	A
	5 _{1,5} – 4 _{1,4}		41987.921±0.030	0.50±0.14	5.83±0.00	1.03±0.22	0.46±0.19	B
	5 _{0,5} – 4 _{0,4}		43027.572±0.030	0.62±0.06	5.83±0.00	1.00±0.00	0.54±0.10	A
	5 _{2,4} – 4 _{2,3}		43152.200±0.030	0.35±0.09	5.83±0.00	0.80±0.00	0.43±0.11	A
	5 _{2,3} – 4 _{2,2}		43290.425±0.030	0.39±0.08	5.83±0.00	0.90±0.18	0.40±0.08	
	5 _{1,4} – 4 _{1,3}		44283.987±0.030	0.38±0.09	5.83±0.00	0.71±0.15	0.50±0.09	
CH ₃ CH ₂ CN	4 _{1,4} – 3 _{1,3}	4-3	34823.952±0.001	0.90±0.09	5.57±0.11	0.80±0.00	1.06±0.06	C
		5-4 & 3-2	34824.090±0.001	1.02±0.09	5.84±0.10	0.80±0.00	1.19±0.06	C,D
	4 _{0,4} – 3 _{0,3}	3-2	35722.142±0.001	0.95±0.06	5.65±0.25	0.80±0.00	1.11±0.08	C
		5-4 & 4-3	35722.239±0.001	1.72±0.06	5.81±0.09	0.70±0.10	2.38±0.08	C,D
	4 _{2,3} – 3 _{2,2}	4-3	35791.730±0.002	0.20±0.06	5.83±0.11	0.69±0.19	0.27±0.08	
		5-4	35792.188±0.001	0.33±0.07	5.81±0.08	0.70±0.16	0.44±0.08	
		3-2	35792.305±0.001	0.22±0.06	5.85±0.08	0.52±0.22	0.39±0.08	
	4 _{2,2} – 3 _{2,1}	4-3	35865.827±0.002	0.32±0.06	6.06±0.11	0.57±0.14	0.52±0.10	E
		5-4	35866.279±0.001	0.25±0.08	5.72±0.08	0.56±0.17	0.42±0.10	E
		3-2	35866.396±0.001	0.33±0.09	5.82±0.08	0.73±0.25	0.42±0.10	E
	4 _{1,3} – 3 _{1,2}	3-2	36379.581±0.001	0.69±0.09	5.71±0.08	0.78±0.12	0.84±0.08	C
		5-4 & 4-3	36379.712±0.001	1.44±0.09	5.78±0.00	0.74±0.05	1.82±0.08	C,D
	5 _{1,5} – 4 _{1,3}	Main	43516.229±0.001	1.76±0.12	5.77±0.03	0.89±0.08	1.86±0.12	D
	5 _{0,5} – 4 _{0,4}	Main	44597.010±0.001	2.86±0.14	5.93±0.02	0.88±0.05	3.05±0.11	D
	5 _{2,3} – 4 _{2,2}	5-4	44877.939±0.001	0.71±0.06	6.13±0.08	1.00±0.22	0.67±0.13	
		6-5 & 4-3	44878.172±0.001	0.73±0.08	5.97±0.08	1.11±0.21	0.62±0.13	D
5 _{1,4} – 4 _{1,3}	Main	45909.544±0.001	1.89±0.12	5.93±0.02	0.78±0.06	2.28±0.10		
CH ₂ CHCCH	4 _{1,4} – 3 _{1,3}		35463.207±0.001	1.76±0.06	5.85±0.01	0.79±0.03	2.10±0.07	
	4 _{0,4} – 3 _{1,0}		36270.155±0.001	2.53±0.06	5.80±0.01	0.77±0.02	3.10±0.06	
	4 _{2,3} – 3 _{2,2}		36298.867±0.001	0.92±0.07	5.77±0.03	0.83±0.07	1.04±0.08	
	4 _{2,2} – 3 _{2,1}		36327.096±0.001	0.60±0.05	5.80±0.03	0.69±0.07	0.83±0.08	
	4 _{1,3} – 3 _{1,2}		37123.615±0.001	1.72±0.07	5.79±0.03	0.69±0.03	2.36±0.06	
	5 _{1,5} – 4 _{1,4}		44323.533±0.001	2.45±0.10	5.82±0.01	0.71±0.04	3.25±0.11	
	5 _{0,5} – 4 _{0,4}		45316.216±0.001	2.54±0.07	5.78±0.01	0.57±0.03	4.19±0.12	
	5 _{2,4} – 4 _{2,3}		45369.726±0.001	1.05±0.09	5.86±0.03	0.63±0.06	1.58±0.12	
	5 _{2,3} – 4 _{2,2}		45426.153±0.001	0.89±0.14	5.85±0.05	0.61±0.10	1.37±0.10	
	5 _{1,4} – 4 _{1,3}		46398.742±0.001	2.49±0.09	5.77±0.01	0.63±0.03	3.70±0.13	
	8 _{0,8} – 7 _{0,7}		72357.946±0.001	8.39±2.23	5.90±0.08	0.58±0.16	13.69±4.21	
	8 _{1,7} – 7 _{1,6}		74197.205±0.001	4.17±1.48	5.54±0.07	0.34±0.12	11.41±3.69	
	9 _{0,9} – 8 _{0,8}		81330.920±0.001	4.56±0.44	5.78±0.03	0.66±0.08	6.52±0.81	
	9 _{1,8} – 8 _{1,7}		83451.437±0.001	3.63±0.33	5.89±0.03	0.61±0.07	5.56±0.67	
	10 _{1,10} – 9 _{1,9}		88558.997±0.001				≤7.53	
	10 _{0,10} – 9 _{0,9}		90279.458±0.001				≤7.59	
	10 _{1,9} – 9 _{1,8}		92698.125±0.001	1.46±0.33	6.19±0.10	0.61±0.13	2.23±0.84	F
CH ₂ CHCN	4 _{1,4} – 3 _{1,3}	4-4	37017.811±0.001	2.42±0.11	5.80±0.02	0.78±0.05	2.90±0.10	
		4-3	37018.828±0.001	30.87±0.15	5.74±0.01	0.73±0.01	39.86±0.10	
		5-4 & 3-2	37018.981±0.001	55.77±0.15	5.91±0.01	0.84±0.01	62.76±0.10	D
		3-3	37020.299±0.001	1.73±0.09	5.80±0.02	0.64±0.04	2.56±0.10	
	4 _{0,4} – 3 _{0,3}	4-4	37903.585±0.001	3.21±0.30	5.80±0.02	0.68±0.07	4.42±0.11	
		3-2	37904.770±0.001	39.15±0.37	5.73±0.03	0.75±0.03	48.98±0.11	
		5-4 & 4-3	37904.880±0.001	95.35±0.38	5.85±0.03	0.72±0.03	124.52±0.11	D
		3-3	37906.477±0.001	1.93±0.06	5.78±0.02	0.58±0.02	3.15±0.11	G
	4 _{2,3} – 3 _{2,2}	4-4 & 4-3	37939.247±0.001	4.87±0.06	5.78±0.01	0.67±0.01	6.80±0.08	
		5-4	37939.764±0.001	6.25±0.07	5.79±0.01	0.71±0.01	8.23±0.08	D
		3-2 & 3-3	37939.897±0.001	3.60±0.07	5.79±0.01	0.66±0.02	5.17±0.08	D
	4 _{2,2} – 3 _{2,1}	4-3 & 4-4	37973.988±0.001	5.73±0.08	5.82±0.01	0.81±0.01	6.67±0.10	D
		5-4	37974.504±0.001	5.97±0.09	5.79±0.01	0.68±0.01	8.30±0.10	
		3-2 & 3-3	37974.634±0.001	3.92±0.09	5.76±0.01	0.71±0.02	5.18±0.10	D
	4 _{1,3} – 3 _{1,2}	4-4	38846.763±0.001	2.03±0.08	5.76±0.01	0.71±0.03	2.70±0.10	
		4-3	38847.641±0.001	31.24±0.12	5.73±0.02	0.70±0.01	41.80±0.10	
	5-4 & 3-2	38847.790±0.001	59.73±0.12	5.87±0.02	0.78±0.01	72.44±0.10	D	
	3-3	38848.933±0.001	2.07±0.07	5.78±0.01	0.64±0.03	3.06±0.10		
1 _{1,0} – 1 _{0,1}	1-0	45332.905±0.001	0.75±0.12	5.74±0.06	0.82±0.18	0.81±0.11		

Table A.1. continued.

Molecule	J^a	F^b	ν_{rest}^c (MHz)	$\int T_A^* dv^d$ (mK km s ⁻¹)	v_{LSR}^e (km s ⁻¹)	Δv^f (km s ⁻¹)	$T_A^* g$ (mK)	Notes
		2-2	45333.979±0.001	1.53±0.10	5.75±0.02	0.56±0.04	2.54±0.11	
		0-1	45334.170±0.001	0.48±0.12	5.73±0.14	0.72±0.08	0.65±0.11	H
		1-2	45334.610±0.001	0.79±0.15	5.81±0.11	1.09±0.20	0.68±0.11	
		2-1	45335.116±0.001	0.60±0.13	5.64±0.07	0.65±0.16	0.87±0.11	
		1-1	45335.747±0.001	0.41±0.09	5.61±0.08	0.58±0.09	0.67±0.11	
	2 _{1,1} – 2 _{0,2}	2-1	45793.994±0.001	0.50±0.06	5.81±0.04	0.65±0.09	0.72±0.10	
		2-3	45794.671±0.001	0.35±0.07	5.60±0.10	0.84±0.20	0.39±0.10	
		1-1	45794.837±0.001	0.92±0.07	5.74±0.02	0.53±0.04	1.63±0.10	
		3-3	45795.213±0.001	2.20±0.06	5.78±0.02	0.63±0.02	3.27±0.10	
		2-2	45795.889±0.001	1.53±0.06	5.76±0.02	0.68±0.03	2.12±0.10	
		3-2	45796.431±0.001	0.49±0.08	5.70±0.09	1.11±0.21	0.42±0.10	
		1-2	45796.732±0.001	0.18±0.05	5.99±0.08	0.53±0.14	0.32±0.10	
	5 _{1,5} – 4 _{1,4}	5-5	46265.718±0.001	0.89±0.09	5.87±0.03	0.56±0.05	1.50±0.14	
		Main	46266.971±0.001	77.60±0.11	6.05±0.01	0.87±0.01	83.80±0.14	D
		4-4	46268.396±0.001	0.87±0.08	5.78±0.03	0.55±0.06	1.50±0.14	
	3 _{1,2} – 3 _{0,3}	2-2	46493.246±0.001	0.81±0.11	5.77±0.03	0.55±0.07	1.37±0.15	
		4-4	46493.381±0.001	2.43±0.06	5.73±0.01	0.61±0.02	3.78±0.15	
		3-3	46493.768±0.001	1.53±0.04	5.75±0.01	0.59±0.03	2.47±0.15	
		4-3	46494.646±0.001	0.52±0.12	6.10±0.13	1.12±0.22	0.44±0.15	H
		2-3	46494.953±0.001	0.87±0.20	5.79±0.20	1.00±0.25	0.82±0.15	H
	5 _{0,5} – 4 _{0,4}	5-5	47353.354±0.001	1.67±0.09	5.84±0.02	0.60±0.04	2.64±0.15	
		Main	47354.670±0.001	112.87±0.10	5.94±0.01	0.75±0.01	142.33±0.15	D
		4-4	47356.233±0.001	1.52±0.09	5.87±0.02	0.61±0.04	2.34±0.15	
	5 _{2,4} – 4 _{2,3}	5-4	47419.606±0.001	5.03±0.13	5.79±0.01	0.62±0.02	7.58±0.18	
		6-5 & 4-3	47419.877±0.001	9.22±0.13	5.74±0.01	0.62±0.02	14.05±0.18	D
	4 _{1,3} – 4 _{0,4}	5-5 & 3-3	47436.292±0.001	3.06±0.11	5.89±0.02	0.74±0.04	3.86±0.10	D
		4-4	47436.559±0.001	1.43±0.08	5.72±0.02	0.58±0.04	2.32±0.10	
	5 _{2,3} – 4 _{2,2}	5-4	47489.042±0.001	5.01±0.04	5.80±0.01	0.62±0.01	7.59±0.18	
		6-5 & 4-3	47489.311±0.001	9.44±0.04	5.73±0.01	0.63±0.01	14.13±0.18	D
	5 _{1,4} – 4 _{1,3}	4-5	48551.488±0.001	1.26±0.16	5.77±0.04	0.60±0.08	1.99±0.22	
		Main	48552.598±0.001	79.78±0.18	6.01±0.01	0.87±0.01	86.41±0.22	D
		4-4	48553.851±0.001	1.24±0.17	5.84±0.04	0.58±0.09	2.03±0.22	
	5 _{1,4} – 5 _{0,5}	4-4 & 6-6	48634.220±0.001	2.39±0.17	5.84±0.03	0.74±0.07	3.05±0.19	D
		5-5	48634.427±0.001	1.70±0.17	5.79±0.04	0.73±0.09	2.19±0.19	
	8 _{1,8} – 7 _{1,7}	Main	73981.555±0.001	39.79±2.58	5.80±0.02	0.53±0.04	70.52±5.36	
	8 _{0,8} – 7 _{0,7}	Main	75585.693±0.001	60.11±1.90	5.78±0.01	0.55±0.02	103.47±3.93	
	8 _{2,7} – 7 _{2,6}	Main	75838.862±0.001	13.07±2.11	5.79±0.04	0.62±0.14	19.67±2.89	H
	8 _{2,6} – 7 _{2,5}	Main	76128.883±0.001	5.25±0.85	5.82±0.03	0.38±0.06	13.14±2.07	
	4 _{1,4} – 3 _{0,3}	3-2	80768.685±0.001	2.30±0.42	5.83±0.01	0.56±0.09	3.86±0.51	
		5-4 & 4-3	80768.827±0.001	5.04±0.44	6.36±0.05	0.65±0.06	7.28±0.51	
	9 _{1,9} – 8 _{1,8}	Main	83207.507±0.001	21.83±0.34	5.80±0.01	0.57±0.01	35.96±0.70	
	9 _{0,9} – 8 _{0,8}	Main	84946.003±0.001	26.90±0.85	5.81±0.01	0.50±0.02	60.18±1.26	
	9 _{2,8} – 8 _{2,7}	Main	85302.649±0.001	5.23±0.95	5.73±0.03	0.35±0.07	13.94±2.51	
	9 _{2,7} – 8 _{2,6}	Main	85715.426±0.001	15.79±3.37	5.75±0.12	1.22±0.22	12.12±2.92	H
	9 _{1,8} – 8 _{1,7}	Main	83712.818±0.001	18.47±1.40	5.82±0.02	0.50±0.04	34.86±3.26	
	5 _{1,4} – 4 _{0,4}	4-3	89130.841±0.001	7.12±1.40	5.70±0.12	1.42±0.04	4.72±3.26	H
	5 _{1,4} – 4 _{0,4}	6-5 & 5-4	89130.919±0.001	2.99±0.99	5.76±0.03	0.37±0.08	7.69±1.37	D,H
	10 _{1,10} – 9 _{1,9}	Main	92426.251±0.001	11.50±0.73	5.80±0.02	0.49±0.03	21.94±1.72	
	10 _{0,10} – 9 _{0,9}	Main	94276.637±0.001	15.45±1.06	5.81±0.02	0.61±0.05	23.89±1.98	
	10 _{2,9} – 9 _{2,8}	Main	94760.783±0.001	3.59±0.59	5.82±0.04	0.49±0.10	6.96±1.23	
	10 _{2,8} – 9 _{2,7}	Main	95325.476±0.001	2.72±0.44	5.91±0.06	0.74±0.16	3.45±0.68	
	10 _{1,9} – 9 _{1,8}	Main	96982.440±0.001	8.04±0.28	5.80±0.01	0.54±0.02	13.96±0.56	
	6 _{1,6} – 5 _{0,5}	Main	97286.826±0.001	4.73±0.35	5.80±0.02	0.60±0.05	7.44±0.66	
	11 _{1,11} – 10 _{1,10}	Main	101637.233±0.001	3.66±0.94	6.01±0.06	0.39±0.14	8.84±2.03	F
	11 _{0,11} – 10 _{0,10}	Main	103575.398±0.001	4.31±1.54	6.03±0.11	0.54±0.18	7.45±3.97	F
	11 _{1,10} – 10 _{1,9}	Main	106641.391±0.001	8.18±1.71	5.67±0.08	0.73±0.18	10.39±3.53	F
¹³ CH ₂ CHCN	4 _{1,4} – 3 _{1,3}	4-3	36058.327±0.001	0.20±0.09	5.47±0.11	0.47±0.42	0.40±0.20	F
	4 _{1,4} – 3 _{1,3}	3-2 & 5-4	36058.479±0.001	0.23±0.32	5.97±0.43	0.58±0.66	0.37±0.20	D
	4 _{0,4} – 3 _{0,3}	3-2	36910.202±0.001	0.33±0.28	5.72±0.27	0.64±0.20	0.48±0.12	
	4 _{0,4} – 3 _{0,3}	4-3 & 5-4	36910.311±0.001	1.06±0.30	5.82±0.10	0.72±0.20	1.39±0.12	D
	4 _{1,3} – 3 _{1,2}	4-3	37815.361±0.001	0.30±0.09	5.76±0.10	0.70±0.21	0.40±0.10	
	4 _{1,3} – 3 _{1,2}	3-2 & 5-4	37815.510±0.001	0.65±0.10	5.86±0.05	0.76±0.08	0.81±0.10	D
	5 _{1,5} – 4 _{1,4}	Main	45066.772±0.001	0.70±0.24	6.21±0.15	0.82±0.33	0.80±0.34	
	5 _{0,5} – 4 _{0,4}	Main	46113.185±0.001	1.21±0.11	5.97±0.03	0.73±0.08	1.57±0.18	
	5 _{1,4} – 4 _{1,3}	Main	47262.702±0.001	0.81±0.13	6.10±0.06	0.76±0.14	1.00±0.21	
CH ₂ ¹³ CHCN	4 _{1,4} – 3 _{1,3}	4-3	36803.089±0.001	0.56±0.53	5.58±0.52	1.17±1.12	0.45±0.15	F, H
	4 _{1,4} – 3 _{1,3}	3-2 & 5-4	36803.242±0.001	0.36±0.28	6.03±0.14	0.62±0.31	0.55±0.15	D, F
	4 _{0,4} – 3 _{0,3}	3-2	37700.144±0.001	0.24±0.23	5.71±0.40	0.76±0.59	0.29±0.12	
	4 _{0,4} – 3 _{0,3}	4-3 & 5-4	37700.255±0.001	0.86±0.24	5.80±0.08	0.65±0.13	1.24±0.12	D
	4 _{1,3} – 3 _{1,2}	4-3	38657.133±0.001	0.41±0.06	6.23±0.07	0.88±0.18	0.43±0.08	H
	4 _{1,3} – 3 _{1,2}	3-2 & 5-4	38657.283±0.001	0.66±0.05	5.88±0.02	0.71±0.03	0.87±0.08	D
	5 _{1,5} – 4 _{1,4}	Main	45996.957±0.001	0.93±0.18	6.14±0.16	1.66±0.40	0.53±0.18	F

Table A.1. continued.

Molecule	J^a	F^b	ν_{rest}^c (MHz)	$\int T_A^* dv^d$ (mK km s ⁻¹)	v_{LSR}^e (km s ⁻¹)	Δv^f (km s ⁻¹)	T_A^{*g} (mK)	Notes
	5 _{0,5} – 4 _{0,4}	Main	47097.459±0.001	0.94±0.10	5.97±0.03	0.65±0.07	1.37±0.16	
	5 _{1,4} – 4 _{1,3}	Main	48314.102±0.001	1.17±0.28	6.13±0.16	1.27±0.35	0.87±0.25	H
CH ₂ CH ¹³ CN	4 _{1,4} – 3 _{1,3}	4-3	36858.005±0.001	0.46±0.09	5.70±0.07	0.65±0.13	0.67±0.08	
	4 _{1,4} – 3 _{1,3}	3-2 & 5-4	36858.158±0.001	0.70±0.10	5.95±0.06	0.82±0.13	0.81±0.08	D
	4 _{0,4} – 3 _{0,3}	3-2	37737.209±0.001	1.08±0.30	5.68±0.14	0.97±0.23	1.04±0.12	
	4 _{0,4} – 3 _{0,3}	4-3 & 5-4	37737.318±0.001	0.95±0.25	5.82±0.05	0.54±0.08	1.64±0.12	D
	4 _{1,3} – 3 _{1,2}	4-3	38672.519±0.001	0.53±0.11	5.76±0.08	0.80±0.20	0.62±0.12	
	4 _{1,3} – 3 _{1,2}	3-2 & 5-4	38672.669±0.001	0.82±0.12	5.85±0.05	0.70±0.10	1.11±0.12	D
	5 _{1,5} – 4 _{1,4}	Main	46066.040±0.002	1.38±0.09	6.01±0.03	0.97±0.07	1.33±0.13	
	5 _{0,5} – 4 _{0,4}	Main	47145.610±0.003	1.95±0.14	5.92±0.03	0.91±0.08	2.02±0.20	
	5 _{1,4} – 4 _{1,3}	Main	48333.801±0.002	1.19±0.14	6.13±0.06	0.89±0.11	1.25±0.22	
CH ₂ CDCN	4 _{1,4} – 3 _{1,3}	4-3	36186.447±0.002	0.19±0.07	5.76±0.07	0.44±0.27	0.41±0.12	F
	4 _{1,4} – 3 _{1,3}	3-2 & 5-4	36186.600±0.002	D, I
	4 _{0,4} – 3 _{0,3}	Main	37227.628±0.002	0.97±0.08	5.87±0.05	0.90±0.13	0.73±0.09	
	4 _{1,3} – 3 _{1,2}	4-3	38369.798±0.002	0.31±0.17	5.73±0.12	0.70±0.28	0.42±0.09	
	4 _{1,3} – 3 _{1,2}	3-2 & 5-4	38369.948±0.002	0.66±0.07	5.82±0.05	1.03±0.08	0.60±0.09	D
	5 _{1,5} – 4 _{1,4}	Main	45221.454±0.002	0.94±0.08	5.90±0.04	1.06±0.11	0.84±0.11	
	5 _{0,5} – 4 _{0,4}	Main	46487.192±0.002	0.59±0.09	5.93±0.06	0.80±0.16	0.70±0.13	
	5 _{1,4} – 4 _{1,3}	Main	47949.865±0.002	0.16±0.07	6.43±0.03	0.24±0.57	0.61±0.16	H
	HCDCHCN	4 _{1,4} – 3 _{1,3}	4-3	35817.812±0.021	0.23±0.05	6.09±0.06	0.52±0.17	0.41±0.09
4 _{1,4} – 3 _{1,3}		3-2 & 5-4	35817.965±0.021	0.28±0.06	5.96±0.07	0.62±0.15	0.43±0.09	D
4 _{0,4} – 3 _{0,3}		Main	36806.410±0.041	0.91±0.12	5.83±0.05	0.84±0.13	1.02±0.15	
4 _{1,3} – 3 _{1,2}		4-3	37882.137±0.021	0.22±0.15	5.44±0.14	0.60±0.28	0.34±0.12	
4 _{1,3} – 3 _{1,2}		3-2 & 5-4	37882.286±0.021	D, I
5 _{1,5} – 4 _{1,4}		Main	44762.173±0.036	0.56±0.19	5.98±0.12	0.72±0.18	0.73±0.12	H
5 _{0,5} – 4 _{0,4}		Main	45967.195±0.070	1.07±0.21	5.98±0.06	0.61±0.12	1.64±0.16	H
5 _{1,4} – 4 _{1,3}		Main	47341.909±0.036	0.27±0.19	6.10±0.32	0.82±0.58	0.31±0.17	F, H
DCHCHCN		4 _{1,4} – 3 _{1,3}	4-3	34701.375±0.014	0.07±0.03	5.80±0.07	0.33±1.37	0.21±0.09
	4 _{1,4} – 3 _{1,3}	3-2 & 5-4	34701.527±0.014	D, I
	4 _{0,4} – 3 _{0,3}	Main	35480.289±0.019	≤0.60	
	4 _{1,3} – 3 _{1,2}	4-3	36302.640±0.014	0.19±0.05	6.40±0.07	0.50±0.13	0.35±0.08	F
	4 _{1,3} – 3 _{1,2}	3-2 & 5-4	36302.789±0.014	0.33±0.06	6.49±0.07	0.78±0.16	0.40±0.08	F, D
	5 _{1,5} – 4 _{1,4}	Main	43371.731±0.029	0.59±0.09	6.32±0.08	0.98±0.14	0.57±0.13	
	5 _{0,5} – 4 _{0,4}	Main	44330.192±0.037	1.12±0.13	6.01±0.05	0.89±0.13	1.19±0.20	
	5 _{1,4} – 4 _{1,3}	Main	45373.023±0.029	0.63±0.18	6.42±0.19	1.26±0.44	0.47±0.22	F
	CH ₂ CHC ¹⁵ N	4 _{1,4} – 3 _{1,3}		35955.662±0.003	0.46±0.07	5.62±0.06	0.74±0.12	0.59±0.09
4 _{0,4} – 3 _{0,3}			36795.189±0.003	J
4 _{1,3} – 3 _{1,3}			37685.857±0.003	0.46±0.10	5.82±0.09	0.83±0.21	0.52±0.13	
5 _{1,5} – 4 _{1,4}			44938.534±0.005	0.40±0.16	5.64±0.15	0.81±0.21	0.46±0.20	F, H
5 _{0,5} – 4 _{0,4}			45970.298±0.007	0.28±0.09	5.87±0.07	0.44±0.17	0.59±0.17	
5 _{1,4} – 4 _{1,3}			45970.298±0.007	I

Notes. ^(a) Rotational quantum numbers.

^(b) Total angular momentum including the spin of N. When "Main" is indicated, it refers to the collapsed hyperfine components with $F_u - F_l = J + 1 \rightarrow J$, $J \rightarrow J - 1$, and $J - 1 \rightarrow J - 2$. In the latter case, the rest frequency corresponds to that of the strongest component.

^(c) Rest frequencies used to derive the v_{LSR} . If the uncertainty on v_{LSR} is zero, then the frequencies correspond to those derived assuming $v_{LSR} = 5.83$ km s⁻¹ (Cernicharo et al. 2020).

^(d) Integrated line intensity in mK km s⁻¹.

^(e) Velocity of the line with respect to the local standard of rest in km s⁻¹.

^(f) Line width at half-intensity using a Gaussian fit in the line profile (in km s⁻¹).

^(g) Antenna temperature (in mK). Upper limits correspond to 3σ values.

^(A) The line is partially blended with an unknown feature (see Fig. 1). The line width has been fixed.

^(B) Data only from the set with frequency-switching throw of 10 MHz.

^(C) Blend of the hyperfine components of the same rotational transition. If the uncertainty on the velocity is zero, then the frequencies were fixed to the predicted ones and the line width was also fixed. The line parameters are correlated. The value for the total integrated intensity of the line, however, is well derived.

^(D) Unresolved hyperfine structure. The frequency of the strongest component was taken as reference. Hence, the derived velocity correspond to an average of the blended hyperfine components.

^(E) Data only from the set with frequency switching throw of 8 MHz.

^(F) Line detected at 3σ level. The line parameters are uncertain.

^(G) Blended with a negative feature produced in the folding of the frequency switching data.

^(H) Blended with another feature. A fit is still possible, but the derived line parameters are uncertain.

^(I) Blended with an unknown feature.

^(J) Blended with CH₃CN.